NeuroImage 291 (2024) 120593

Contents lists available at ScienceDirect

NeuroImage

journal homepage: www.elsevier.com/locate/ynimg

Detection of individual brain tau deposition in Alzheimer's disease based on latent feature-enhanced generative adversarial network

Jiehui Jiang [a,1,*], Rong Shi [b,1], Jiaying Lu [c,d,1], Min Wang [a,*], Qi Zhang [b], Shuoyan Zhang [b], Luyao Wang [a], Ian Alberts [e], Axel Rominger [e], Chuantao Zuo [c,d,f,**], Kuangyu Shi [e,g], for the Alzheimer's Disease Neuroimaging Initiative

[a] Institute of Biomedical Engineering, School of Life Sciences, Shanghai University, Shanghai, China
[b] School of Information and Communication Engineering, Shanghai University, Shanghai, China
[c] Department of Nuclear Medicine & PET Center, Huashan Hospital, Fudan University, Shanghai, China
[d] National Research Center for Aging and Medicine and National Center for Neurological Disorders, Huashan Hospital, Fudan University, Shanghai, China
[e] Department of Nuclear Medicine, Inselspital, University of Bern, Bern, Switzerland
[f] Human Phenome Institute, Fudan University, Shanghai, China
[g] Department of Informatics, Technical University of Munich, Munich, Germany

ARTICLE INFO

Keywords:
Alzheimer's disease
Generative adversarial network
Standardized uptake value ratio
^{18}F-flortaucipir tau Positron emission tomograph
^{18}F-florzolotautau Positron emission tomography

ABSTRACT

Objective: The conventional methods for interpreting tau PET imaging in Alzheimer's disease (AD), including visual assessment and semi-quantitative analysis of fixed hallmark regions, are insensitive to detect individual small lesions because of the spatiotemporal neuropathology's heterogeneity. In this study, we proposed a latent feature-enhanced generative adversarial network model for the automatic extraction of individual brain tau deposition regions.

Methods: The latent feature-enhanced generative adversarial network we propose can learn the distribution characteristics of tau PET images of cognitively normal individuals and output the abnormal distribution regions of patients. This model was trained and validated using 1131 tau PET images from multiple centres (with distinct races, i.e., Caucasian and Mongoloid) with different tau PET ligands. The overall quality of synthetic imaging was evaluated using structural similarity (SSIM), peak signal to noise ratio (PSNR), and mean square error (MSE). The model was compared to the fixed templates method for diagnosing and predicting AD.

Results: The reconstructed images archived good quality, with SSIM = 0.967 ± 0.008, PSNR = 31.377 ± 3.633, and MSE = 0.0011 ± 0.0007 in the independent test set. The model showed higher classification accuracy (AUC = 0.843, 95 % CI = 0.796−0.890) and stronger correlation with clinical scales (r = 0.508, P < 0.0001). The model also achieved superior predictive performance in the survival analysis of cognitive decline, with a higher hazard ratio: 3.662, P < 0.001.

Interpretation: The LFGAN4Tau model presents a promising new approach for more accurate detection of individualized tau deposition. Its robustness across tracers and races makes it a potentially reliable diagnostic tool for AD in practice.

1. Introduction

Alzheimer's disease (AD) is a common neurodegenerative disease characterized by a progressive decline in multiple cognitive domains. Pathological changes appear decades before the onset of the disease, and the prodromal stage may exhibit highly heterogeneous clinical manifestations. Positron emission tomography (PET) imaging is a crucial part of this biomarker detection, as it allows for the identification of intraneuronal aggregates of hyperphosphorylated, misfolded tau protein (neurofibrillary tangles, NFTs). Tau PET offers extensive visualization and quantification that is unmatched at the histopathological level and the tau PET can support from the detection of Braak stages to

* Corresponding authors at: Institute of Biomedical Engineering, School of Life Sciences, Shanghai University, Shanghai, China.
** Corresponding author at: Department of Nuclear Medicine & PET Center, Huashan Hospital, Fudan University, Shanghai, China.
E-mail addresses: jiangjiehui@shu.edu.cn (J. Jiang), wmwin@shu.edu.cn (M. Wang), zuochuantao@fudan.edu.cn (C. Zuo).
[1] These authors contributed equally to this work.

https://doi.org/10.1016/j.neuroimage.2024.120593
Received 27 November 2023; Received in revised form 17 March 2024; Accepted 25 March 2024
Available online 28 March 2024

the heterogeneity of tau pathology found in the literature (Ossenkoppele et al., 2016, Schöll et al., 2016, Sintini et al., 2019), and tau PET imaging is now widely used in the diagnosis of AD (Hall et al., 2017, Schwarz et al., 2018).

The common approaches for interpreting tau PET imaging mainly consist of visual assessment (Lin et al., 2023, Seibyl et al., 2023, Sonni et al., 2020) and semi-quantitative analysis in the regions of interest (ROIs) related to the disease (Jack et al., 2020, Leuzy et al., 2021, Lu et al., 2023a , Mathoux et al., 2024, Provost et al., 2021). Specifically, the visual assessment method, although it can incorporate individual differences, is subjective in some cases of atypical tau distributions and ambiguity. On the other hand, the semi-quantitative analysis method relies on manual segmentation and fixed templates (Provost et al., 2021), and with accumulated evidence of the various spatiotemporal tau patterns and trajectories, a simple region-specific quantification of tau PET can be considered to be less effective (Hong et al., 2022). Moreover, both visual assessment and manual segmentation methods require significant time and effort, and the fixed templates approach is insensitive to the detection of small lesions (Aksman et al., 2021, Vogel et al., 2021, Young et al., 2018). To address the above issues, researchers have proposed deep learning models, such as U-net (Ronneberger et al., 2015), DeepMedic (Kamnitsas et al., 2016), variational autoencoder (VAE) (Chen and Konukoglu, 2018) and generative adversarial network (GAN) (Baur et al., 2021) to overcome the limitations of conventional methods. The primary advantage of deep learning is that it can reduce manual work, such as image preprocessing, segmentation of regions of interest, feature extraction and fusion. However, the focus of deep learning models is to learn the distribution of labelled data, which might overlook individual differences and various tau deposition patterns, Additionally, healthy subjects may show elevated signals due to off-target binding (Zhang et al., 2021a), rendering deep learning-based individual deposition detection models for tau PET imaging unavailable at present. Then we pay attention to the unsupervised anomaly detection residual strategy method that has been applied to MRI images (Chen and Konukoglu, 2018). This method does not need data label training; and can adapt to diverse types of anomalies. Compared with traditional deep learning training strategies, it also has better generalization ability.

Therefore, we propose a data-driven unsupervised model aimed at overcoming issues related to individual heterogeneity and indistinct discrimination of normal tau signals, thereby enabling precise identification of abnormal deposition regions within individual images. Specifically, we enhance the latent layer distribution constraint of the conventional GAN model, introducing a method termed LFGAN4Tau, a Latent Feature-Enhanced Generative Adversarial Network method. Through unsupervised training on a substantial dataset of cognitively normal individuals' tau PET images, our model is capable of mapping patient images onto cognitively normal reference images and accurately locating non-normal deposited areas by comparison with the original images. Moreover, we aspire to demonstrate the potential clinical diagnostic value of our proposed model through clinical diagnosis, prediction, and its correlation with clinical assessments.

2. Subjects/materials and methods

2.1. Participants

This retrospective study was approved by the Institutional Review Committee of the Alzheimer's Disease Neuroimaging Initiative (ADNI) and Huashan Hospital (Ethics approval code for Huashan Hospital: KY2018-363, KY2019-551, KY2020-043, KY2021-555), and written informed consent was obtained from each participant or legal guardian. A total of 1086 participants, including subjects from ADNI and Huashan Hospital, were included in this study. Of note, the majority of participants in ADNI were Caucasian and all subjects from Huashan Hospital were Mongoloid. Cohort 1 consisted of 483 cognitively normal (CN) individuals, 204 patients with early mild cognitive impairment (EMCI), 194 patients with late mild cognitive impairment (LMCI), and 107 patients with AD from ADNI. Detailed information regarding participant enrollment in ADNI can be found at https://adni.loni.usc.edu. All participants in the ADNI received baseline ^{18}F-flortaucipir tau PET scans, T1-weighted structural Magnetic resonance imaging (MRI) scans, and related clinical information, including Apolipoprotein E (ApoE) status, scores of Mini-Mental State Examination (MMSE), Clinical Dementia Rating-Sum of Boxes (CDR-SB), Montreal Cognitive Assessment (MOCA), Alzheimer's Disease Assessment-11 (ADAS11), ADAS13, and ADASQ4. 436 subjects in Cohort 1 (44.1 %) underwent β-Amyloid PET scans using ^{18}F-florbetapir. The whole-brain β-Amyloid Standardized uptake value ratio (SUVR) values provided by ADNI were used to classify β-Amyloid abnormal (A+) and β-Amyloid normal (A−) status (threshold: 1.18) (Chen et al., 2015, Zhang et al., 2022). Additionally, 110 patients and 27 CNs in Cohort 1 had longitudinal tau PET scans with a mean follow-up of 20.8 months, and 25 of them met the criteria for progressive cognitive deterioration (Chen et al., 2021) (defined as (a) diagnosis of dementia or (b) MMSE $\leq$ 24 at the last visit or (c) decline of MMSE value$\geq$4 between the first visit and the last visit within 2 years). The flowchart illustrating the inclusion and exclusion of participants in Cohort 1 is provided in (Fig. S1).

Additionally, Cohort 2 was enrolled as an independent test dataset, comprising 29 CN individuals and 69 patients with AD from Huashan Hospital (Shanghai, China). All participants received baseline ^{18}F-florzolotau (also known as ^{18}F-PM-PBB3, ^{18}F-APN-1607) tau PET scans (Li et al., 2021, Zhang et al., 2022), T1-weighted structural MRI scans, and MMSE scores. The diagnosis of AD patients in Huashan was based on the 2011 NIA-AA criteria (Frisoni et al., 2011), and additionally, CDR-SB and MOCA assessments were performed.

For the subsequent training and testing of the anomaly detection model, the CNs in Cohort 1 were split into the train group and the validation group, by the ratio of 7:3 and stratified sampling according to both sex and age. AD patients in Cohort 1 were defined the as AD-ADNI group, CNs and AD patients in Cohort 2 were defined as the CN- Huashan and AD-Huashan groups, respectively. In addition, we trained additional models (T−) on tau PET negative subjects in the CN-ADNI (see the Model Training section of the supplementary material for details).

2.2. Imaging acquisition and preprocessing

For the ADNI dataset, the raw ^{18}F-flortaucipir PET images and T1-weighted structural MRI were downloaded from the official ADNI website (https://adni.loni.usc.edu/) and subsequently preprocessed uniformly. For the Huashan dataset, ^{18}F-florzolotau PET imaging and T1-weighted structural MRI were obtained as previously reported (Li et al., 2021). Subjects underwent anatomical MRI using a 3.0-T horizontal magnet (Discovery MR750; GE Medical Systems, Milwaukee, WI), followed by ^{18}F-florzolotau PET imaging. High-resolution T1-weighted images were acquired with the following parameters: TE of 3.2 milliseconds, TR of 8.2 milliseconds, TI of 450 milliseconds, flip angle of 12°, acquisition matrix of 256 × 256 × 152, and voxel size of 1 × 1 × 1 mm. Huashan Hospital utilized a Siemens mCT Flow PET/CT scanner (Siemens, Erlangen, Germany) in 3-D mode to acquire PET images. To correct for attenuation, a low-dose CT transmission scan was conducted. Participants received 370 MBq of ^{18}F-florzolotau intravenously and rested for 90 minutes before the 20-minute imaging acquisition (90-110 minutes). The images were reconstructed using a 3-D ordered-subset expectation maximization algorithm (4 iterations; 24 subsets; Gaussian filter, 2 mm; zoom, 3) and resulted in a matrix size of 256 × 256 × 148 and a voxel size of 2 × 2 × 3 mm^3.

All PET images were pre-processed using the Statistical Parametric Mapping toolbox in MATLAB 2016b. Firstly, each PET image was co-registered with the corresponding T1 image. Then, the transformation parameters standardized in T1-weighted MRI image standardization were used to convert the PET image to Montreal Neurological Institute (MNI) space. To increase the signal-to-noise ratios, the images were

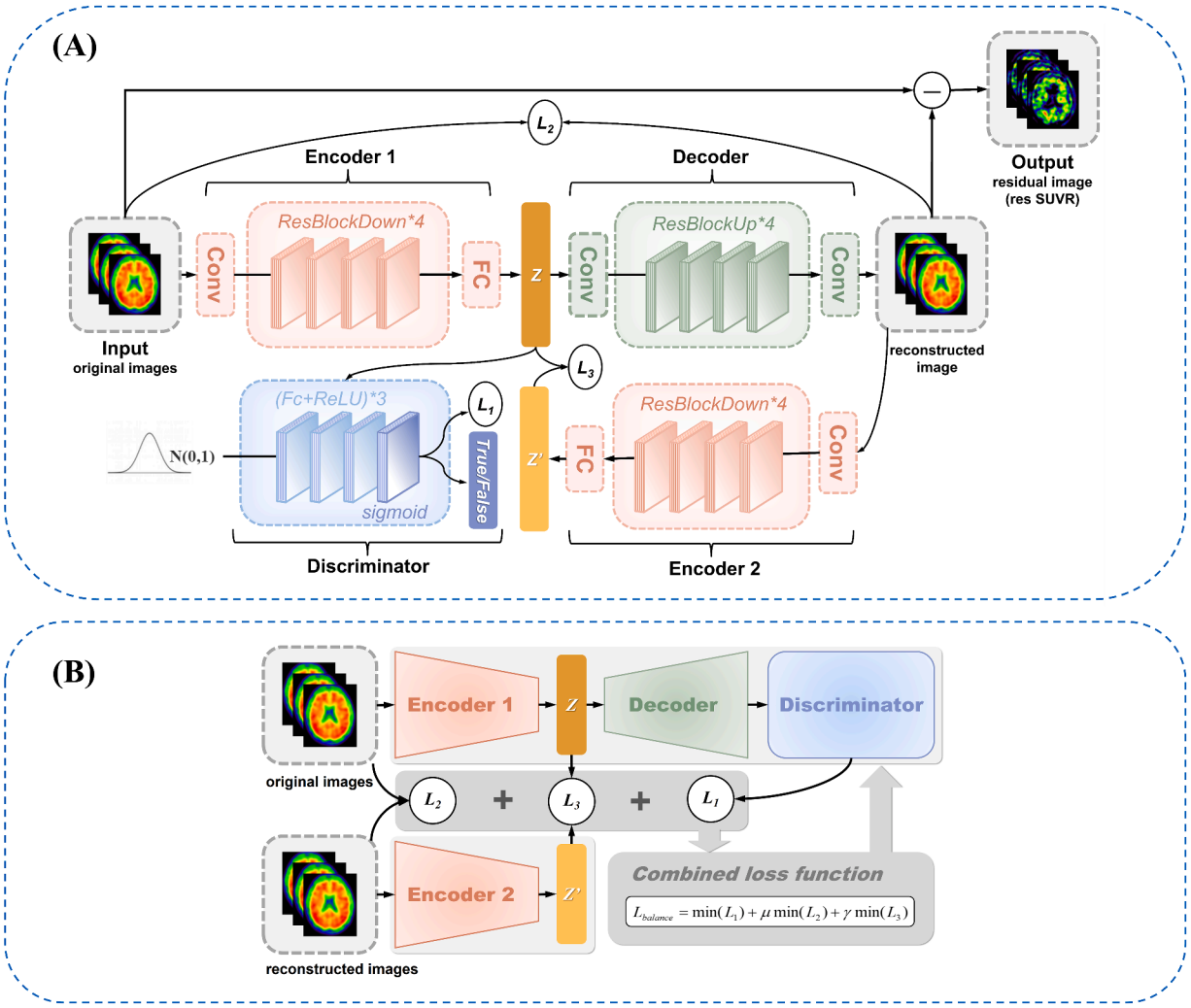

Fig. 1. Model Introduction. (A) The architecture of the LFGAN4Tau. (B) Construction of loss functions.

smoothed with an 8 mm full width at half maximum Gaussian kernel and resampled to a voxel size of 2 × 2 × 2 mm^3.

To clarify, the study used the cerebellar grey matter (Automated Anatomical Labeling atlas 3, AAL3 NO.95,96 brain regions) as the reference brain region to calculate the SUVR map for tau PET imaging. The tau SUVRs were quantified in a meta-ROI consisting of several brain regions using the AAL3 template, including the hippocampus, inferior temporal lobe, lingual gyrus, middle temporal lobe, occipital lobe, parahippocampus, parietal lobe, posterior cingulate gyrus, precuneus and fusiform (Chotipanich et al., 2020), Additionally, three Braak staging ROIs (Braak 1&2, Braak 3&4, Braak 5&6) were defined using Freesurfer (Yan et al., 2021).

2.3. Network architecture of LFGAN4Tau

The LFGAN4Tau model is based on a combination of GAN and VAE, as described in previous studies (Baur et al., 2021, Chen and Konukoglu, 2018, Shi et al., 2023). The input of the model is a tau PET image slice, as a result, the output is a residual map of the tau deposition region obtained by the residual strategy. The overall structure of the model consists of two encoders, a decoder, and a discriminator (Fig. 1 A).

The training objective of the LFGAN4Tau model is aligned with the min-max equation of GAN, which is presented in (1) (Goodfellow et al., 2020, Islam and Zhang, 2020, Kang et al., 2018):

$$\min_{G}\max_{D} V(D,G) = E_{z\sim p(z)}[logD(z)] + E_{z\sim q(z)}[\log(1-D(z))] \quad (1)$$

where ***D*** is Discriminator, ***G*** is Generator, z denotes a latent variable, $p(z)$ is a prior distribution, in this case, a Gaussian distribution, and $q(z)$ is the encoder's distribution function. More details can be found in the supplementary material.

$$\mathscr{L}_{balance} = \min(\mathscr{L}_1) + \mu\min(\mathscr{L}_2) + \gamma\min(\mathscr{L}_3) \quad (2)$$

$$\mathscr{L}_1 = E_{z\sim q(z)} - E_{z\sim P(z)}D(z) + \lambda E_{z\sim P(penalty)}[\max(0, \| \nabla_z D(x) \| - 1)]$$

$$\mathscr{L}_2 = |x - x'|$$

$$\mathscr{L}_3 = |z - z'|^2$$

To solve the problem of individual heterogeneity and non-pathological tau PET tracer signals discrimination in tau PET images, we effectively regulated the potential constraint terms by combining the encoding of normal distributions in the model with a special multiple loss function (Fig. 1 B), which has been utilized in similar studies before (Shi et al., 2023, Shi et al., 2022). This regularization preserved the individual characteristics of the subjects and ultimately facilitated the detection of individual heterogeneity and pathological tau deposition. The primary loss function is $\mathscr{L}1$, as stated in (2). $P(penalty)$ denotes the intermediate distribution of the two distributions, and λ is set to 10 by default. Furthermore, the pixel difference between the generated and original images is represented by $\mathscr{L}2$. Additionally, the consistency of $\mathscr{L}3$ in potential vectors serves as an auxiliary loss function to the GAN

Table 1
Demographics and characteristics

	Cohort 1 (ADNI)				Cohort 2 (Huashan)	
	CN-ADNI (Train/Validation)	EMCI	LMCI	AD-ADNI	CN-Huashan (Test)	AD-Huashan
Gender(M/F)	186/297*,†,‡	115/89*	113/81†	68/39‡	11/18	25/44
Age(years)	72.38±8.42†,‡	73.45±7.38	74.33±7.75†	74.57±7.71‡	57.75±7.95	61.65±10.33
Education	16.67±2.23‡	16.31±2.76	16.51±2.39	15.50±2.56‡	9.62±3.02	10.17±3.96
MMSE	29.01±1.69*,†,‡	28.00±1.99*	27.35±2.26†	21.83±4.17‡	27.52±2.31	19.52±7.15
MOCA-B	26.12±2.64*,†,‡	23.79±3.23*	22.80±3.65†	17.01±4.67‡	/	13.30±6.33
CDR-SB	0.05±0.18*,†,‡	1.31±1.20*	1.56±1.07†	5.38±2.71‡	/	7.30±3.63
ADAS11	5.21±2.67*,†,‡	8.48±4.11*	10.29±4.48†	19.86±7.62‡	/	/
ADAS13	8.21±4.19*,†,‡	13.45±6.27*	16.64±6.81†	30.41±9.25‡	/	/
ADASQ4	2.56±1.82*,†,‡	4.32±2.40*	5.56±2.50†	8.79±1.58‡	/	/
APOE carriers	157(36.51%)*,†,‡	80(44.69%)*	77(49.68%)†	56(60.22%)‡	/	/
Amyloid-β +	67(29.13%)†,‡	41(42.71%)	44(55.00%)†	26(86.67%)‡	/	/

Note: The data were given as mean standard ± SD or number (%). ADNI: Alzheimer Disease Neuroimaging Initiative, CN: cognitively normal, EMCI: early mild cognitive impairment, LMCI: late mild cognitive impairment, AD: Alzheimer's disease, MMSE: Mini-Mental State Examination, MOCA-B: Basic Version of Montreal Cognitive Assessment, CDR-SB: Clinical Dementia Rating-Sum of Boxes, ADAS: Alzheimer's Disease Assessment.

* $P < 0.05$, comparison between CN-ADNI and EMCI.

† $P < 0.05$, comparison between CN-ADNI and. LMCI.

‡ $P < 0.05$, comparison between CN-ADNI and AD.

base loss function, ensuring better quality image recovery and feature retention.

2.4. Overall quality assessment of reconstructed images

To assess the overall quality of the model involved comparing reconstructed images to original images in the Train, Validation, and Test groups, three index indicators were used: the structural similarity (SSIM) (Wang et al., 2004), peak signal-to-noise ratio (PSNR), and mean square error (MSE) (Shi et al., 2023). Furthermore, to demonstrate the superiority of the multiple loss functions, we conducted ablation experiments in the same Train, Validation and Test groups by training the model without $\mathscr{L}1$, $\mathscr{L}2$, or $\mathscr{L}3$ loss functions, respectively. Furthermore, we also calculated the SUVR of individual detected tau deposited area, in other words, using the voxels defined by the residual images to calculate an SUVR (defined as residual SUVR).

2.5. Visualization of the outcome by LFGAN4Tau

We utilized both visualization and quantitative analysis methods to examine the direct output of the model. To aid in visualization, we selected several representative subjects at different stages of disease progression, displaying their tau PET images, clinical information, as well as the generated and residual images produced by the model. Subsequently, a conservative threshold of 0.01 was applied to binarize the residual images (more details of the results for different thresholds are available in the Supplementary Material), and the residual SUVR values were calculated and compared with fixed templates SUVR values for different clinical groups. Traditional SUVR values were calculated using ROIs comprising: 1) whole brain; 2) meta-ROI; 3) Braak 1&2; 4) Braak 3&4; and 5) Braak 5&6. Box scatter plots were employed to demonstrate the differences between clinical groups and A+/A− subgroups in CN-ADNI-Val, EMCI, LMCI, AD-ADNI, CN-Huashan and AD-Huashan groups.

2.6. Classification experiments

To assess the classification performance of the residual SUVR, the comparison was made between residual SUVR and fixed templates SUVR values by conducting Receiver Operating Characteristic (ROC) analysis and computing Hedges' g effect sizes in the Validation, EMCI, LMCI, AD-ADNI, and AD-Huashan groups. Specifically, we compared the SUVR values derived from the template for conventional tau deposition regions (including the 5 brain regions mentioned in the previous section) with the residual SUVR value obtained from LFGAN4Tau. We calculated the mean and 95 % confidence interval of the ROC curve and used Hedges' g effect sizes to quantify the magnitude of the difference between the two groups.

2.7. Statistical analysis

We conducted non-parametric rank sum tests to compare the demographic and clinical characteristics of subjects in the CN and disease groups. Additionally, we utilized one-way ANOVA tests to compare the residual SUVR values generated from the LFGAN4Tau model segmentation of tau-precipitated brain regions with fixed templates SUVR values between each clinical disease group and corrected the differences between groups using Tukey's multiple comparisons tests. To evaluate the impact of differentiation on disease conversion prediction, we employed the log-rank test to assess the survival difference between the high-risk and low-risk groups. We performed all statistical analyses using SPSS 25.0 and considered the level of significance to be $P < 0.05$.

We conducted correlation analyses to examine the association between residual SUVR and fixed templates SUVR and clinical scores of disease severity. The analysis was carried out using Spearman's correlation coefficient in the CN-ADNI-Val, EMCI, LMCI, and AD-ADNI groups in Cohort 1. The clinical indicators used in the analysis were MMSE, MOCA-B, CDR-SB, ADAS11, ADAS13, and ADASQ4.

To analyze the ability of the model to predict the risk of cognitive decline in patients with CN or MCI, we constructed a Cox proportional hazards model using longitudinal data from ADNI. We separated the data into low-risk and high-risk groups based on the upper quartile of output risk value as the threshold and used the Kaplan-Meier (KM) method for survival analysis of different groups with an endpoint event defined as progressive cognitive deterioration.

3. Results

3.1. Subject characteristics

The CN group in Cohort 1 had significant differences in gender, MMSE, MOCA-B, CDR-SB, ADAS, and APOE4 status compared to the other three groups ($P < 0.0001$). Furthermore, there were significant age differences and β-Amyloid status between the CN group and LMCI and AD groups ($P < 0.0001$). Lastly, the CN and AD groups exhibited a significant difference in education years ($P = 0.0001$) (Table 1). The demographics and characteristics of the A+/A− subgroup are shown in Table S1.

Table 2
The results of objective indicators.

Model	Group	SSIM	PSNR	MSE
LFGAN4Tau	Train	0.979±0.009	36.215±3.987	0.0004±0.0005
	Validation	0.975±0.009	34.996±3.909	0.0005±0.0004
	Test	**0.967±0.008**	**31.377±3.633**	**0.0011±0.0007**
L1+L2	Train	0.970±0.010	35.057±3.519	0.0005±0.0004
	Validation	0.972±0.010	35.182±3.821	0.0005±0.0004
	Test	0.966±0.008	31.251±3.683	0.0011±0.0007
L1+L3	Train	0.921±0.022	31.535±2.346	0.0010±0.0006
	Validation	0.923±0.025	31.110±2.325	0.0010±0.0005
	Test	0.913±0.030	28.606±1.921	0.0017±0.0006
L2+L3	Train	0.967±0.011	34.371±3.020	0.0005±0.0005
	Validation	0.964±0.010	33.369±3.023	0.0006±0.0004
	Test	0.955±0.009	30.523±3.506	0.0012±0.0008

Note: The SSIM, PSNR, and MSE of each group are presented as mean ± standard. Bold indicates the maximum value in the Test set. The Train and Validation sets are from ADNI, Test set is from Huashan. SSIM: structural similarity (higher values indicate better image similarity), PSNR: peak signal to noise ratio (higher values indicate better image quality), MSE: mean square error (lower values indicate better image quality), LFGAN4Tau: a Latent Feature-Enhanced Generative Adversarial Network method proposed in this paper, L1+L2, L1+L3, L2+L3 represent LFGAN4Tau models without L3, L2, L1 loss functions respectively.

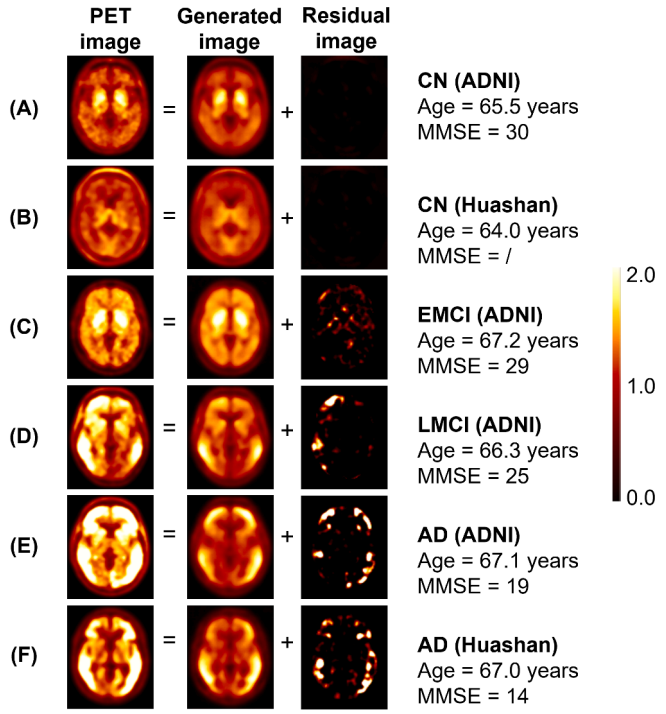

Fig. 2. Examples of generated images and residual images.

3.2. Overall quality assessment of reconstructed images

Images from the CN group were used to validate the overall quality of the model reconstruction. The objective indicators in our model perform better on both the ADNI Train and Validation groups than other models, and also on the data from the external validation group, Huashan hospital with different tau tracer (^{18}F-florzolotau), SSIM can reach 0.967 ± 0.009, PSNR reaches 31.377 ± 3.633, and MSE is 0.0011 ± 0.0007 (Table 2). In addition, ablation experiments (Table 2) and comparative model results (Table S2) show that our proposed model with multiple loss functions has the best performance. Detailed results of the LFGAN4Tau(T−) model are shown in the Model Training section of the supplementary material.

3.3. Visualization of the outcome by LFGAN4Tau

We present examples of images generated by the LFGAN4Tau model (Fig. 2; Fig. S6), and the LFGAN4Tau(T−) model (Fig. S7), with all participants of comparable ages. On an individual level, the residual image for each subject outlined distinct brain regions. In general, the residual brain region exhibited a more diffuse pattern as the disease severity progressed. Moreover, In Fig. 2, our residual SUVRs are more discriminatory across diseases, which suggests that these individual regions from our model provided a better characterization of tau uptake values, which may be valuable for clinical applications.

Both residual SUVR and fixed templates SUVR showed differential distribution across the disease groups, with SUVR values increasing with disease progression and higher in A+ patients than in A− patients (Fig. 3 A). The residual SUVR values displayed a more discrete and differentiated distribution. A post-hoc test revealed that residual SUVR was significantly different in the four groups: CN vs. LMCI ($P < 0.001$), CN vs. AD ($P < 0.0001$), EMCI vs. AD ($P < 0.0001$) and LMCI vs. AD ($P < 0.0001$). The data distribution of A+/− subgroups (Fig. 3 B) showed significant differences in residual SUVR in the five groups: CN(A−) vs. MCI(A+) ($P < 0.0001$), CN(A−) vs. AD(A+) ($P < 0.0001$), CN(A+) vs. AD(A+) ($P < 0.01$), MCI(A−) vs. MCI(A+) ($P < 0.0001$) and MCI(A−) vs. AD(A+) ($P < 0.0001$). In the distribution of data in the Huashan cohort, all six groups were significantly different in CN vs. AD ($P < 0.0001$) (Fig. 3 C). The specific P values are shown in Table S3.

3.4. Classification experiments

The residual SUVR from the LFGAN4Tau model exhibited relatively good discriminatory power (Table 3). Within the clinical subgroups, residual SUVR values showed the highest area under the curve (AUC) values in CN vs. AD (AUC = 0.843, 95 % confidence interval (CI) = 0.796−0.890), EMCI vs. AD (AUC = 0.736, 95 % CI = 0.681−0.791), and LMCI vs. AD (AUC = 0.708, 95 %CI = 0.650−0.766). In the A+/− subgroup analysis (Table S4), residual SUVR values achieved the highest AUC values in the AD(A+) group vs. CN(A−), CN(A+), MCI(A−), MCI (A+), AD(A−). Additionally, in the CN vs. AD ROC analysis of the Huashan cohort, residual SUVR values yielded the best results (AUC = 0.983, 95 %CI = 0.967−1.000).

3.5. Correlations with clinical scores for disease severity

This study included CN-ADNI-Val (n = 145), MCI (n = 398), and AD-ADNI (n = 107) data from ADNI. The individual residual SUVR values were found to have a significant correlation with various cognitive assessments such as MMSE ($r = -0.432$, $P < 0.0001$), CDR-SB ($r = 0.4038$, $P < 0.0001$), MOCA-B ($r = -0.4573$, $P < 0.0001$), ADAS11 ($r = 0.4646$, $P < 0.0001$), ADAS13 ($r = 0.5082$, $P < 0.0001$) and ADASQ4 ($r = 0.4832$, $P < 0.0001$) (Fig. 4; Fig. S4). These correlations were found to be stronger compared to those obtained from fixed templates SUVR values. Additionally, in the separate correlation results between the CN and disease groups (MCI & AD), it was interestingly found that res SUVR values had the strongest correlation in the disease group ($r = 0.4898$, $P < 0.0001$), while the correlation was poorer in the CN group ($r = 0.2440$, $P = 0.0032$).

3.6. Survival analysis

Based on the definition of endpoint events, the rate of progressive cognitive deterioration was 18.25 %, detailed longitudinal data are shown in Table S5. The LFGAN4Tau model exhibited a higher predictive power (hazard ratio = 3.662, 95 % CI: 1.815–7.385) compared to the other SUVRs. Furthermore, the Braak SUVRs were non-significant in the COX regression analysis ($P > 0.05$) (Fig. 5).

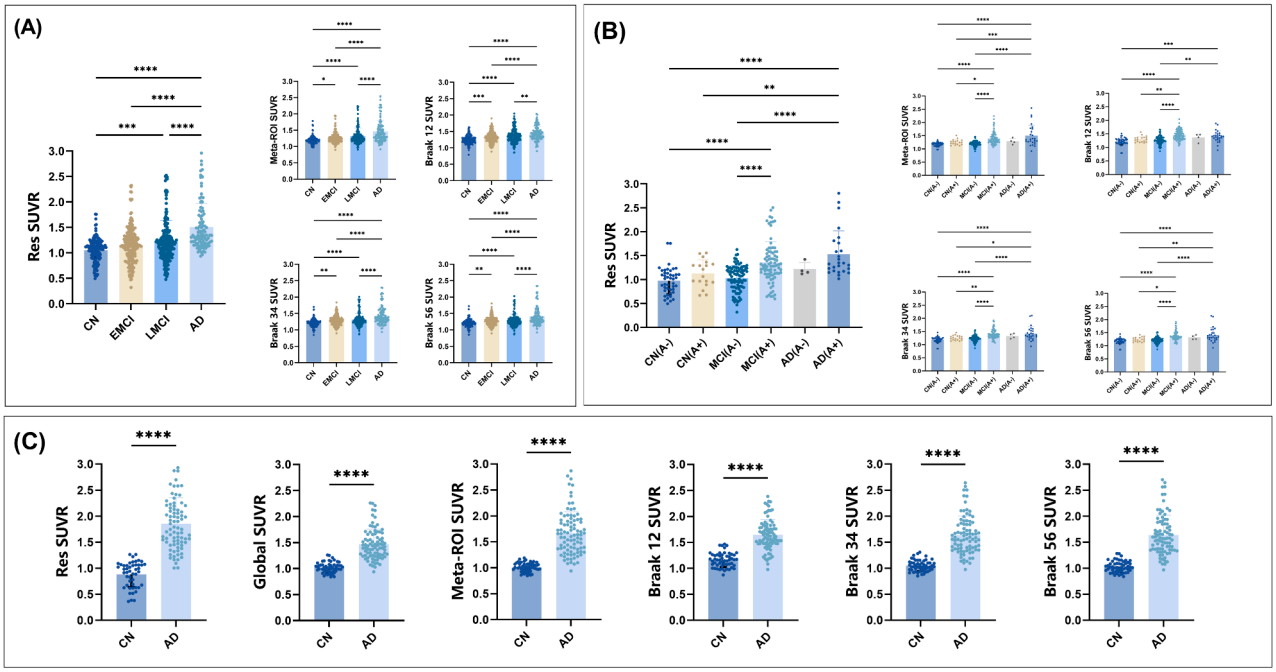

Fig. 3. Residual SUVR and fixed templates SUVR values for different grouping situations. (A) Data distribution with clinical subgroups. (B) Data distribution for A+/− subgroups. (C) Data distribution under the Huashan group.

Table 3
Results of ROC Analysis in clinical subgroups.

	Residual SUVR	Global SUVR	Meta-ROI SUVR	Braak 1&2 SUVR	Braak 3&4 SUVR	Braak 5&6 SUVR
CN-ADNI-Val vs. EMCI	0.591±0.030 (0.0039)	0.637±0.030 (<0.0001)	0.646±0.029 (<0.0001)	0.649±0.029 (<0.0001)	**0.653±0.029 (<0.0001)**	0.652±0.029 (<0.0001)
CN-ADNI-Val vs. LMCI	0.619±0.030 (0.0002)	0.625±0.030 (<0.0001)	0.675±0.029 (<0.0001)	**0.676±0.029 (<0.0001)**	0.664±0.029 (<0.0001)	0.653±0.030 (<0.0001)
CN-ADNI-Val vs. AD-ADNI	**0.843±0.024 (<0.0001)**	0.758±0.032 (<0.0001)	0.803±0.030 (<0.0001)	0.785±0.030 (<0.0001)	0.791±0.030 (<0.0001)	0.785±0.030 (<0.0001)
EMCI vs. LMCI	0.532±0.029 (0.2690)	0.508±0.029 (0.7897)	**0.541±0.029 (0.1531)**	0.535±0.029 (0.2260)	0.514±0.029 (0.6322)	0.504±0.029 (0.8884)
EMCI vs. AD-ADNI	**0.736±0.028 (<0.0001)**	0.645±0.034 (<0.0001)	0.703±0.033 (<0.0001)	0.653±0.033 (<0.0001)	0.666±0.033 (<0.0001)	0.662±0.033 (<0.0001)
LMCI vs. AD-ADNI	**0.708±0.029 (<0.0001)**	0.644±0.034 (<0.0001)	0.656±0.034 (<0.0001)	0.615±0.034 (0.0009)	0.648±0.033 (<0.0001)	0.654±0.033 (<0.0001)
CN-Huashan vs. AD-Huashan	**0.983±0.009 (<0.0001)**	0.959±0.015 (<0.0001)	0.981±0.010 (<0.0001)	0.940±0.019 (<0.0001)	0.973±0.012 (<0.0001)	0.973±0.012 (<0.0001)

Note: ROC results are expressed as: area under the curve AUC ± Std. Error (*P* value). Bold indicates the maximum value of the AUC. ROC: Receiver operating characteristic, CN: cognitively normal, EMCI: early mild cognitive impairment, LMCI: late mild cognitive impairment, AD: Alzheimer's disease, Val: Validation, SUVR: semi-quantitative uptake value ratios.

4. Discussion

In this study, we proposed a LFGAN4Tau method for individual tau deposition, which aimed to facilitate clinicians in achieving better diagnosis and prediction for AD.

The LFGAN4Tau model utilizes adversarial generation techniques to map a patient's tau PET distribution onto that of a CN individual. The underlying mechanism involves the collaborative learning of the model's generator and discriminator. This process yields reconstructed images, which can be roughly considered as the patient's tau PET image before the onset of cognitive impairment. The discrepancies between these reconstructed images and the original images can be leveraged to derive regions of tau deposition. To solve the problem of individual heterogeneity and non-pathological tau deposition discrimination in tau PET images, we added a multiple loss function. This multifarious loss function serves a dual purpose: first, to reinforce the constraints on latent features, thereby steering the model toward generating more accurate and meaningful outputs; and second, to equip the model with the adaptability needed to accommodate the inherent diversity in image characteristics.

The residual images obtained from the proposed method were distributed in AD-related brain regions (Fig. 2 C-F), which generally

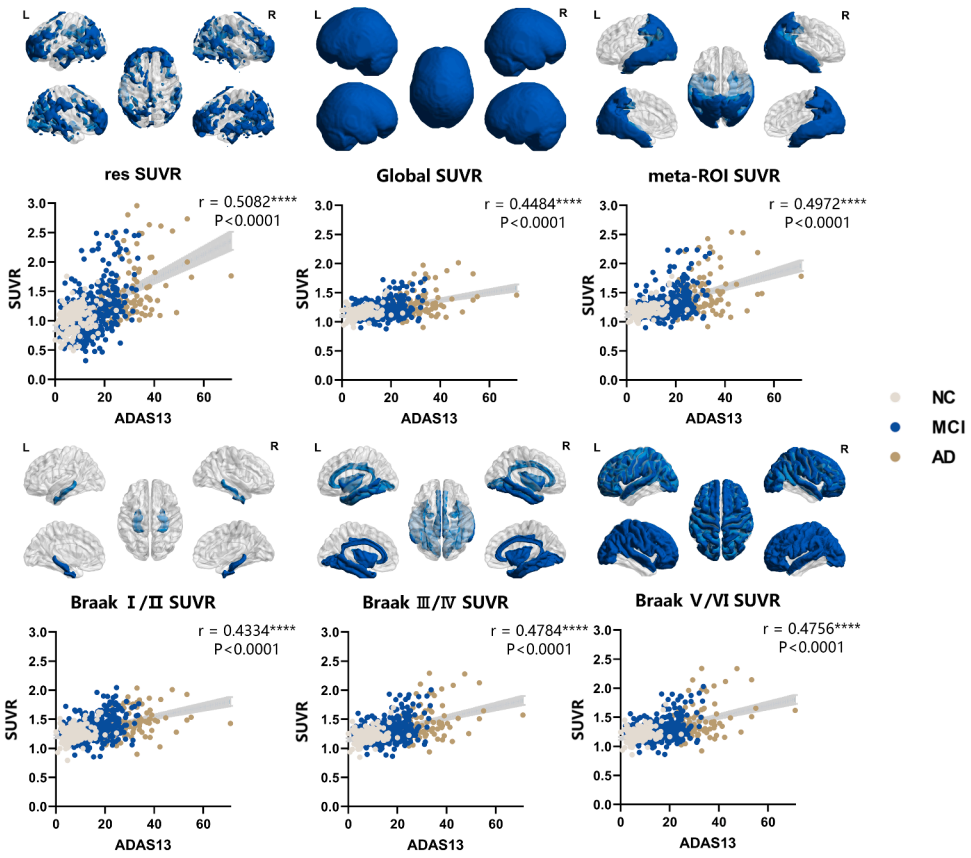

Fig. 4. Correlations between ADAS13 clinical scores and different SUVR values of tau images.

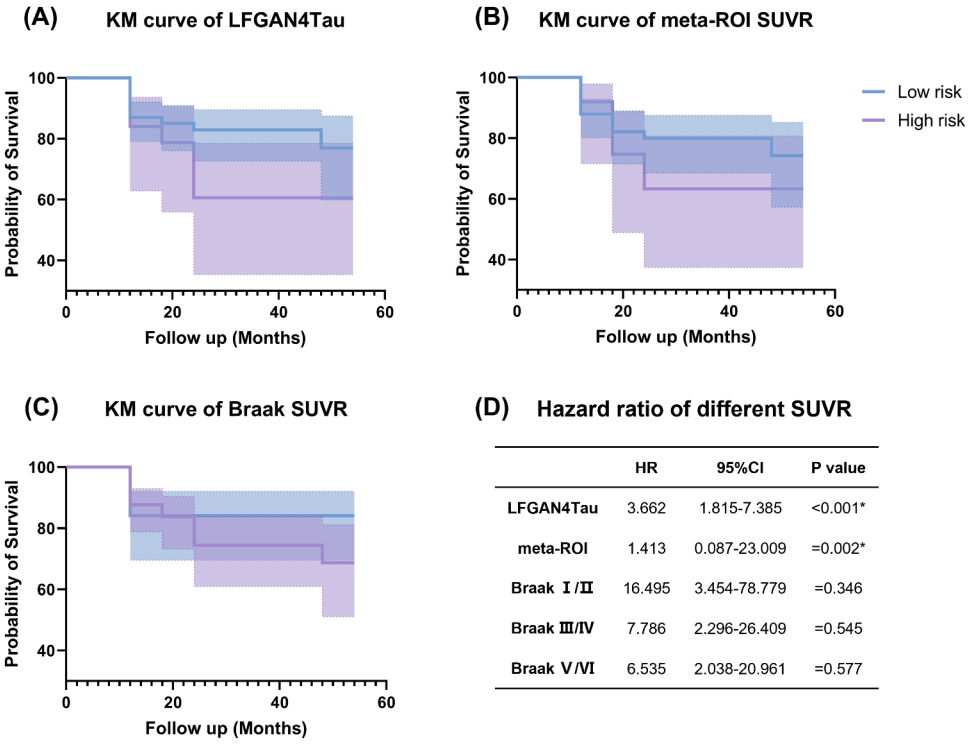

(D) Hazard ratio of different SUVR

	HR	95%CI	P value
LFGAN4Tau	3.662	1.815-7.385	<0.001*
meta-ROI	1.413	0.087-23.009	=0.002*
Braak Ⅰ/Ⅱ	16.495	3.454-78.779	=0.346
Braak Ⅲ/Ⅳ	7.786	2.296-26.409	=0.545
Braak Ⅴ/Ⅵ	6.535	2.038-20.961	=0.577

Fig. 5. Hazard ratios for different predictors and Kaplan–Meier survival curves.

Table 4
Correlation between ADAS13 clinical scores and different SUVR values of tau images (in the CN group, and disease group respectively).

	Residual SUVR	*Global SUVR*	*Meta-ROI SUVR*	*Braak 1&2 SUVR*	*Braak 3&4 SUVR*	*Braak 5&6 SUVR*
CN-ADNI-Val	0.2440 (0.0032)	0.3513 (<0.0001)	**0.4213 (<0.0001)**	0.3082 (0.0002)	0.3515 (<0.0001)	0.3585 (<0.0001)
MCI & AD-ADNI	**0.4898 (<0.0001)**	0.4121 (<0.0001)	0.4551 (<0.0001)	0.3798 (<0.0001)	0.4365 (<0.0001)	0.437 (<0.0001)

Note: Correlations results are expressed as: r value (P value). Bold indicates the maximum value of the r value.

followed the widely accepted pathological model of tau trajectory (Hong et al., 2022, Leuzy et al., 2019). However, abnormalities in tau accumulation reflected by the elevated signals were more prominent and easier to identify than the original images due to the clearance of interfering signals from off-target/non-specific binding (Whittington and Gunn, 2019, Whittington and Gunn, 2021). In most participants, the areas of abnormal tau deposition captured by residual images were consistent with a traditional limbic-predominant phenotype with a Braak-like spatial progression (Fig. 2). Residual images also indicated that there is a non-negligible number of subjects exhibiting heterogeneity in tau patterning, consistent with previous findings (Lu et al., 2023b, Vogel et al., 2021, Young et al., 2022), such as frontal and parietal-dominant (Fig. S6 A), asymmetric pattern (Fig. S6 B-C), and our residual images show "atypical" tau trajectories. Furthermore, since tau accumulation is heterogeneous not only in different regions but also within the same region, the ability to describe the precise extent of tau deposition and provide weighted intensity calculations displayed by residual images could help to avoid underestimation caused by mean calculations. Taken together, while the fixed templates SUVR values may not accurately reflect the individualized tau deposition, the proposed residual SUVRs could facilitate precise disease tracking regardless of variation in tau pathology.

We initially assessed the clinical utility of this model in tau PET imaging for diagnosis, and our method demonstrated improved performance compared to the fixed template method in classifying different entities and binary amyloid statuses (A+/A−) in most cases, especially in the mid-disease phase. We then evaluated its efficiency on disease prognosis, and the proposed method consistently outperformed the fixed template method. The observed superior predictive performance in survival analysis for cognitive decline, with a higher hazard ratio (3.662, $P < 0.001$) indicates the model's promising prognostic value in AD. These improvements re-emphasized the importance of accounting for individual heterogeneity when interpreting tau PET imaging in practice (Leuzy et al., 2019, Zhang et al., 2021b). Of note, although our LFGAN4Tau model was solely trained in the ^{18}F-flortaucipir PET imaging from ADNI, it was independently tested not only on the same scans but also on a different tau PET imaging (^{18}F-florzolotau) in another race. The solid performance in both tests to some extent confirmed the satisfactory generalizability of the current approach.

Beyond its diagnostic role, tau PET imaging holds promise as a biomarker of disease severity in AD (Chen et al., 2021). Accurate quantification of tau deposits requires consideration of both extent and intensity. Although the fixed template method takes into account the most commonly involved regions in AD, averaging the signal over a uniform range would partially reduce the accuracy of this marker in reflecting the extent of the disease, which would further affect the precise assessment of disease progression and treatment efficacy at the individual level. As expected, the new tau biomarker residual SUVR obtained from our model showed better classification and prediction performances, and stronger associations in disease groups with clinical scales than SUVR values in meta-ROIs (both anatomical and pathological ROIs) in AD. Although its superiority remains to be tested in future clinical trials, the results now show the feasibility of using deep learning models to detect individual small lesions and identify new tau PET biomarkers in AD.

Overall, our LFGAN4Tau method showed promising results and provided a new perspective for tau PET image detection and quantification. Nonetheless, this work has some limitations. Firstly, our modified model used registered and smoothed SUVR images, which could have reduced the detailed information of the tau PET scan. Although raw images without registration and smoothing could be more appropriate for deep learning model training, it would require higher computing power and more training data. We fully recognise that the computational efficiency aspect has not been sufficiently considered in the current study. We have not been able to fully discuss the computational efficiency and scalability of the models, especially in terms of their actual deployment in clinical practice. We do consider deploying the model on better GPUs or large-scale computing platforms in the future to improve computational efficiency and accelerate the model run speed. Secondly, the model is currently more sensitive to classifying the disease in the middle and later stages, which may be because the tau pathology is not obvious enough in the early stages, and the image voxels are less distributed, which may directly result in the poorer correlation of res SUVR with ADAS13 in the CN group (Table 4). In the future, we will consider how to optimise the model with fewer voxels. In the survival analysis, more neurodegenerative markers will be compared in the future to make the study more complete. Finally, although we used data from two centres in our study, we are also aware that this may not be sufficient to cover all cases, and that the smaller number of CNs at the Huashan centre has an age difference from the ADNI data. We plan to further expand our data sources and collect data from more centres for validation in future studies to more fully assess the robustness and generalisation ability of the model. As a deep learning model, LFGAN4Tau still has some black box attributes. Although we have demonstrated the interpretability of the results using multiple methods, they cannot be used as the only evidence for diagnosis, and can only be used as an auxiliary diagnostic tool currently. Future work will focus on enhancing the interpretability and generalization performance of the model and exploring its potential applications in other medical image analysis tasks.

CRediT authorship contribution statement

Jiehui Jiang: Writing – review & editing, Writing – original draft, Supervision, Methodology, Investigation, Conceptualization. **Rong Shi:** Writing – review & editing, Writing – original draft, Visualization, Software, Investigation, Formal analysis, Data curation. **Jiaying Lu:** Writing – review & editing, Validation, Supervision, Resources, Funding acquisition, Conceptualization. **Min Wang:** Writing – review & editing, Validation, Supervision, Project administration. **Qi Zhang:** Software, Investigation, Data curation. **Shuoyan Zhang:** Visualization, Supervision, Software. **Luyao Wang:** Supervision, Project administration, Methodology. **Ian Alberts:** Visualization, Resources, Project administration. **Axel Rominger:** Writing – review & editing, Validation, Resources, Project administration. **Chuantao Zuo:** Writing – review & editing, Supervision, Resources, Project administration, Methodology. **Kuangyu Shi:** Writing – review & editing, Validation, Supervision, Resources, Project administration, Methodology.

Declaration of competing interest

There are no conflicts of interest including any financial, personal, or other relationships with people or organizations for any of the authors related to the work described in the manuscript.

Data availability

This study used data from two cohorts: Alzheimer's Disease Neuroimaging Initiative (ADNI) and Huashan Hospital. The data of the ADNI cohort were originally from the online repository of the ADNI database (http://adni.loni.usc.edu/), which is easily available to the research public. The data from the Huashan cohort generated during processing and analysis are available from the corresponding author upon reasonable request.

Acknowledgement statement

We would like to thank the Zuo Chuantao research team for their help in data collection and management as well as the dedication of each research participant. This work was supported by the Natural Science Foundation of China (grant number: 62206165, 62376150, 62303295).

Supplementary materials

Supplementary material associated with this article can be found, in the online version, at doi:10.1016/j.neuroimage.2024.120593.

References

Aksman, L.M., Wijeratne, P.A., Oxtoby, N.P., Eshaghi, A., Shand, C., Altmann, A., Alexander, D.C., Young, A.L., 2021. pySuStaIn: a Python implementation of the Subtype and Stage Inference algorithm. SoftwareX 16.

Baur, C., Denner, S., Wiestler, B., Navab, N., Albarqouni, S., 2021. Autoencoders for unsupervised anomaly segmentation in brain MR images: a comparative study. Med. Image Anal. 69, 101952.

Chen, K., Roontiva, A., Thiyyagura, P., Lee, W., Liu, X., Ayutyanont, N., Protas, H., Luo, J.L., Bauer, R., Reschke, C., Bandy, D., Koeppe, R.A., Fleisher, A.S., Caselli, R.J., Landau, S., Jagust, W.J., Weiner, M.W., Reiman, E.M., 2015. Improved power for characterizing longitudinal amyloid-beta PET changes and evaluating amyloid-modifying treatments with a cerebral white matter reference region. J. Nucl. Med. 56, 560–566.

Chen, S.D., Lu, J.Y., Li, H.Q., Yang, Y.X., Jiang, J.H., Cui, M., Zuo, C.T., Tan, L., Dong, Q., Yu, J.T., Alzheimer's Disease Neuroimaging, I., 2021. Staging tau pathology with tau PET in Alzheimer's disease: a longitudinal study. Transl. Psychiatry 11, 483.

Chen, X., Konukoglu, E., 2018. Unsupervised detection of lesions in brain MRI using constrained adversarial auto-encoders.

Chotipanich, C., Nivorn, M., Kunawudhi, A., Promteangtrong, C., Boonkawin, N., Jantarato, A., 2020. Evaluation of Imaging Windows for Tau PET Imaging Using (18) F-PI2620 in Cognitively Normal Individuals, Mild Cognitive Impairment, and Alzheimer's Disease Patients. Mol. ImAging 19, 1536012120947582.

Frisoni, G.B., Winblad, B., O'Brien, J.T., 2011. Revised NIA-AA criteria for the diagnosis of Alzheimer's disease: a step forward but not yet ready for widespread clinical use. Int. Psychogeriatr. 23, 1191–1196.

Goodfellow, I., Pouget-Abadie, J., Mirza, M., Xu, B., Warde-Farley, D., Ozair, S., Courville, A., Bengio, Y., 2020. Generative adversarial networks. Commun. ACM 63, 139–144.

Hall, B., Mak, E., Cervenka, S., Aigbirhio, F.I., Rowe, J.B., O'Brien, J.T., 2017. In vivo tau PET imaging in dementia: pathophysiology, radiotracer quantification, and a systematic review of clinical findings. Ageing Res. Rev. 36, 50–63.

Hong, J., Shi, K., Rominger, A., Choi, H., 2022. Image-level trajectory inference of tau pathology using variational autoencoder for Flortaucipir PET. Eur. J. Nucl. Med. Mol. ImAging 49, 3061–3072.

Islam, J., Zhang, Y., 2020. GAN-based synthetic brain PET image generation. Brain Inform. 7, 3.

Jack, C.R., Wiste, H.J., Weigand, S.D., Therneau, T.M., Lowe, V.J., Knopman, D.S., Botha, H., Graff-Radford, J., Jones, D.T., Ferman, T.J., Boeve, B.F., Kantarci, K., Vemuri, P., Mielke, M.M., Whitwell, J., Josephs, K., Schwarz, C.G., Senjem, M.L., Gunter, J.L., Petersen, R.C., 2020. Predicting future rates of tau accumulation on PET. Brain 143, 3136–3150.

Kamnitsas, K., Ferrante, E., Parisot, S., Ledig, C., Nori, A.V., Criminisi, A., Rueckert, D., Glocker, B., 2016. DeepMedic for Brain Tumor Segmentation. In: Crimi, A., Menze, B., Maier, O., Reyes, M., Winzeck, S., Handels, H. (Eds.), Brainlesion: Glioma, Multiple Sclerosis, Stroke and Traumatic Brain Injuries. Springer International Publishing, Athens, Greece, pp. 138-149.

Kang, S.K., Seo, S., Shin, S.A., Byun, M.S., Lee, D.Y., Kim, Y.K., Lee, D.S., Lee, J.S., 2018. Adaptive template generation for amyloid PET using a deep learning approach. Hum. Brain Mapp. 39, 3769–3778.

Leuzy, A., Chiotis, K., Lemoine, L., Gillberg, P.G., Almkvist, O., Rodriguez-Vieitez, E., Nordberg, A., 2019. Tau PET imaging in neurodegenerative tauopathies-still a challenge. Mol. Psychiatry 24, 1112–1134.

Leuzy, A., Pascoal, T.A., Strandberg, O., Insel, P., Smith, R., Mattsson-Carlgren, N., Benedet, A.L., Cho, H., Lyoo, C.H., La Joie, R., Rabinovici, G.D., Ossenkoppele, R., Rosa-Neto, P., Hansson, O., 2021. A multicenter comparison of [18F]flortaucipir, [18F]RO948, and [18F]MK6240 tau PET tracers to detect a common target ROI for differential diagnosis. Eur. J. Nucl. Med. Mol. ImAging 48, 2295–2305.

Li, L., Liu, F.-T., Li, M., Lu, J.-Y., Sun, Y.-M., Liang, X., Bao, W., Chen, Q.-S., Li, X.-Y., Zhou, X.-Y., Guan, Y., Wu, J.-J., Yen, T.-C., Jang, M.-K., Luo, J.-F., Wang, J., Zuo, C., Progressive Supranuclear Palsy, N., 2021. Clinical Utility of F-18-APN-1607 Tau PET Imaging in Patients with Progressive Supranuclear Palsy. Movement Disord. 36, 2314–2323.

Lin, H.C., Lin, K.J., Huang, K.L., Chen, S.H., Ho, T.Y., Huang, C.C., Hsu, J.L., Chang, C.C., Hsiao, I.T., 2023. Visual reading for [18F]Florzolotau ([18F]APN-1607) tau PET imaging in clinical assessment of Alzheimer's disease. Front. Neurosci. 17.

Lu, J.Y., Ju, Z.Z., Wang, M., Sun, X., Jia, C.H., Li, L., Bao, W.Q., Zhang, H.W., Jiao, F.Y., Lin, H.M., Yen, T.C., Cui, R.X., Lan, X.L., Zhao, Q.H., Guan, Y.H., Zuo, C.T., Shanghai Memory Study, S.M.S., 2023a. Feasibility of 18F-florzolotau quantification in patients with Alzheimer's disease based on an MRI-free tau PET template. Eur. Radiol. 33, 4567–4579.

Lu, J.Y., Zhang, Z.W., Wu, P., Liang, X.N., Zhang, H.W., Hong, J.M., Clement, C., Yen, T. C., Ding, S.N., Wang, M., Xiao, Z.X., Rominger, A., Shi, K.Y., Guan, Y.H., Zuo, C.T., Zhao, Q.H., 2023b. The heterogeneity of asymmetric tau distribution is associated with an early age at onset and poor prognosis in Alzheimer's disease. Neuroimage-Clin. 38.

Mathoux, G., Boccalini, C., Peretti, D.E., Arnone, A., Ribaldi, F., Scheffler, M., Frisoni, G. B., Garibotto, V., 2024. A comparison of visual assessment and semi-quantification for the diagnostic and prognostic use of [18F]flortaucipir PET in a memory clinic cohort. Eur. J. Nucl. Med. Mol. ImAging.

Ossenkoppele, R., Schonhaut, D.R., Schöll, M., Lockhart, S.N., Ayakta, N., Baker, S.L., O'Neil, J.P., Janabi, M., Lazaris, A., Cantwell, A., Vogel, J., Santos, M., Miller, Z.A., Bettcher, B.M., Vossel, K.A., Kramer, J.H., Gorno-Tempini, M.L., Miller, B.L., Jagust, W.J., Rabinovici, G.D., 2016. Tau PET patterns mirror clinical and neuroanatomical variability in Alzheimer's disease. Brain 139, 1551–1567.

Provost, K., Iaccarino, L., Soleimani-Meigooni, D.N., Baker, S., Edwards, L., Eichenlaub, U., Hansson, O., Jagust, W., Janabi, M., La Joie, R., Lesman-Segev, O., Mellinger, T.J., Miller, B.L., Ossenkoppele, R., Pham, J., Smith, R., Sonni, I., Strom, A., Mattsson-Carlgren, N., Rabinovici, G.D., Alzheimer's Disease Neuroimaging, I., 2021. Comparing ATN-T designation by tau PET visual reads, tau PET quantification, and CSF PTau181 across three cohorts. Eur. J. Nucl. Med. Mol. ImAging 48, 2259–2271.

Ronneberger, O., Fischer, P., Brox, T., 2015. U-Net: convolutional networks for biomedical image segmentation. In: Navab, N., Hornegger, J., Wells, W.M., Frangi, A.F. (Eds.), Medical Image Computing and Computer-Assisted Intervention – MICCAI 2015. Springer International Publishing, Munich, Germany, pp. 234-241.

Schöll, M., Lockhart, S.N., Schonhaut, D.R., O Neil, J.P., Janabi, M., Ossenkoppele, R., Baker, S.L., Vogel, J.W., Faria, J., Schwimmer, H.D., Rabinovici, G.D., Jagust, W.J., 2016. PET imaging of tau deposition in the aging human brain. Neuron 89, 971–982.

Sr. Schwarz, A.J., Shcherbinin, S., Slieker, L.J., Risacher, S.L., Charil, A., Irizarry, M.C., Fleisher, A.S., Southekal, S., Joshi, A.D., Devous, M.D., Miller, B.B., Saykin, A.J., Alzheimer's Disease Neuroimaging, I., 2018. Topographic staging of tau positron emission tomography images Alzheimers. Dement. (Amst.) 10, 221–231.

Seibyl, J.P., DuBois, J.M., Racine, A., Collins, J., Guo, Q., Wooten, D., Stage, E., Cheng, D. V., Gunn, R.N., Porat, L., Whittington, A., Kuo, P.H., Ichise, M., Comley, R., Martarello, L., Salinas, C., 2023. A visual interpretation algorithm for assessing brain tauopathy with 18F-MK-6240 PET. J. Nucl. Med. 64, 444–451.

Shi, R., Sheng, C., Jin, S., Zhang, Q., Zhang, S., Zhang, L., Ding, C., Wang, L., Wang, L., Han, Y., Jiang, J., 2023. Generative adversarial network constrained multiple loss autoencoder: a deep learning-based individual atrophy detection for Alzheimer's disease and mild cognitive impairment. Hum. Brain Mapp. 44, 1129–1146.

Shi, R., Wang, L., Jiang, J., 2022. Alzheimer's Disease Neuroimaging, I., 2022. An unsupervised region of interest extraction model for tau PET images and its application in the diagnosis of Alzheimer's disease. In: 44th Annual International Conference of the IEEE Engineering in Medicine & Biology Society (EMBC), pp. 2157–2160.

Sintini, I., Martin, P.R., Graff-Radford, J., Senjem, M.L., Schwarz, C.G., Machulda, M.M., Spychalla, A.J., Drubach, D.A., Knopman, D.S., Petersen, R.C., Lowe, V.J., Jack, C.R., Josephs, K.A., Whitwell, J.L., 2019. Longitudinal tau-PET uptake and atrophy in atypical Alzheimer's disease. Neuroimage-Clin. 23.

Sonni, I., Segev, O.H.L., Baker, S.L., Iaccarino, L., Korman, D., Rabinovici, G.D., Jagust, W.J., Landau, S.M., La Joie, R., 2020. Evaluation of a visual interpretation method for tau-PET with 18F-flortaucipir. Alzheimer's & Dement. 12.

Vogel, J.W., Young, A.L., Oxtoby, N.P., Smith, R., Ossenkoppele, R., Strandberg, O.T., La Joie, R., Aksman, L.M., Grothe, M.J., Iturria-Medina, Y., Pontecorvo, M.J., Devous, M.D., Rabinovici, G.D., Alexander, D.C., Lyoo, C.H., Evans, A.C., Hansson, O., 2021. Four distinct trajectories of tau deposition identified in Alzheimer's disease. pp. 871-881.

Wang, Z., Bovik, A.C., Sheikh, H.R., Simoncelli, E.P., 2004. Image quality assessment: from error visibility to structural similarity. Ieee Trans. Image Process. 13, 600–612.

Whittington, A., Gunn, R.N., 2019. Amyloid Load: A More Sensitive Biomarker for Amyloid Imaging. J. Nucl. Med. 60, 536–540.

Whittington, A., Gunn, R.N., Alzheimer's Disease Neuroimaging, I., 2021. Tau(IQ): a canonical image based algorithm to quantify Tau PET scans. J. Nucl. Med. 62, 1292–1300.

Yan, S., Zheng, C., Paranjpe, M.D., Li, Y., Li, W., Wang, X., Benzinger, T.L., Lu, J., Zhou, Y.J.B., 2021. Sex modifies APOE ε4 dose effect on brain tau deposition in cognitively impaired individuals. 144, 3201-3211.

Jr Young, A.L., Marinescu, R.V., Oxtoby, N.P., Bocchetta, M., Yong, K., Firth, N.C., Cash, D.M., Thomas, D.L., Dick, K.M., Cardoso, J., van Swieten, J., Borroni, B., Galimberti, D., Masellis, M., Tartaglia, M.C., Rowe, J.B., Graff, C., Tagliavini, F., Frisoni, G.B., Laforce, R., Finger, E., de Mendonca, A., Sorbi, S., Warren, J.D., Crutch, S., Fox, N.C., Ourselin, S., Schott, J.M., Rohrer, J.D., Alexander, D.C., Genetic, F.T.D.I., Alzheimer's Disease Neuroimaging, I., 2018. Uncovering the heterogeneity and temporal complexity of neurodegenerative diseases with Subtype and Stage Inference. Nat. Commun. 9, 4273.

Young, C.B., Winer, J.R., Younes, K., Cody, K.A., Betthauser, T.J., Johnson, S.C., Schultz, A., Sperling, R.A., Greicius, M.D., Cobos, I., Poston, K.L., Mormino, E.C., 2022. Divergent cortical tau positron emission tomography patterns among patients with preclinical Alzheimer disease. JAMa Neurol. 79, 592–603.

Zhang, K., Mizuma, H., Zhang, X., Takahashi, K., Jin, C., Song, F., Gao, Y., Kanayama, Y., Wu, Y., Li, Y., Ma, L., Tian, M., Zhang, H., Watanabe, Y., 2021.. PET imaging of neural activity, beta-amyloid, and tau in normal brain aging. Eur. J. Nucl. Med. Mol. Imaging 48, 3859–3871.

Zhang, W., Xu, S., Yu, H., Li, X., Jin, Z., Li, Y., He, Z., 2021.. Radioactive synthesis of tau PET imaging agent (18)F-AV-1451 and its role in monitoring the progression of Alzheimer's disease and supporting differential diagnosis. Ann. Nucl. Med. 35, 139–147.

Zhang, Y., Lu, J., Wang, M., Zuo, C., Jiang, J., 2022. Influence of gender on tau precipitation in Alzheimer's disease according to ATN research framework. Phenomics.